

Robustness of Quantum Criticality of Valence Fluctuations

Shinji WATANABE¹ and Kazumasa MIYAKE²

¹*Department of Basic Sciences, Kyushu Institute of Technology, Kitakyushu, Fukuoka
804-8550, Japan*

²*Toyota Physical and Chemical Research Institute, Nagakute, Aichi 480-1192, Japan*

The mechanism of emergence of robust quantum criticality in Yb- and Ce-based heavy electron systems under pressure is analyzed theoretically. By constructing a minimal model for quasicrystal $\text{Yb}_{15}\text{Al}_{34}\text{Au}_{51}$ and its approximant, we show that quantum critical points of the first-order valence transition of Yb appear in the ground-state phase diagram with their critical regimes being overlapped to be unified, giving rise to a wide quantum critical regime. This well explains the robust unconventional criticality observed in $\text{Yb}_{15}\text{Al}_{34}\text{Au}_{51}$ under pressure. We also discuss broader applicability of this mechanism to other Yb- and Ce-based systems such as $\beta\text{-YbAlB}_4$ showing unconventional quantum criticality.

KEYWORDS: robust quantum criticality, valence fluctuation, unconventional criticality, Yb- and Ce-based heavy electrons, quasicrystal

Quantum critical phenomena, which do not follow conventional spin fluctuation theory,¹⁻⁴⁾ have attracted much attention in condensed matter physics. Unconventional criticality commonly observed in paramagnetic metal phase in heavy-electron systems YbRh_2Si_2 ⁵⁾ and $\beta\text{-YbAlB}_4$ ⁶⁾ challenges a paradigm of the magnetic quantum criticality (see Table I).

Recently, it has been clarified theoretically by the present authors that critical valence fluctuation of Yb is the key origin of emergence of the new type of quantum criticality.⁷⁾ We have found that almost dispersionless critical valence-fluctuation mode appears near $\mathbf{q}=\mathbf{0}$ in momentum space because of strong Coulomb repulsion of 4f holes at the Yb site. This gives rise to an extremely small characteristic temperature of critical valence fluctuations, T_0 with $T_0 \ll T_K$ where T_K is a characteristic temperature of heavy-electron systems, i.e., the so-called Kondo temperature. This makes experimentally-accessible low-temperature regime be located at “high-temperature” $T/T_0 \gg 1$ regime, which is the origin of emergence of anomalous criticality in physical quantities.⁷⁾ Depending on the flatness of the critical valence fluctuation mode, the uniform magnetic susceptibility χ and the NMR/NQR relaxation rate $(T_1T)^{-1}$ shows $\chi \propto (T_1T)^{-1} \sim T^{-\zeta}$ with $0.5 \lesssim \zeta \lesssim 0.7$. As shown in Table I, quantum

valence criticality gives a unified explanation for the measured unconventional criticality.

Recently, newly synthesized heavy-electron metal $\text{Yb}_{15}\text{Al}_{34}\text{Au}_{51}$ with quasicrystal structure has been revealed to exhibit the common unconventional criticality.^{8,9)} It has been reported that low-temperature behavior of χ , $(T_1T)^{-1}$, specific-heat coefficient C/T , and resistivity ρ is well explained by the theory of quantum valence criticality, as shown in Table I.⁸⁾ This discovery suggests ubiquity of quantum valence criticality. The key origin is considered to be the locality of the critical valence fluctuation mode, which is basically ascribed to atomic origin at the Yb site not depending on the detail of lattice structures such as periodic lattice or quasicrystal.

In Table I, $\beta\text{-YbAlB}_4$ and $\text{Yb}_{15}\text{Al}_{34}\text{Au}_{51}$ show the quantum critical behavior without tuning control parameters such as pressure, magnetic field, or chemical doping. Here we have the following interesting question: Is it accidental or inevitable? To answer this question, we consider that a recent measurement may give a hint: Quantum criticality observed in $\text{Yb}_{15}\text{Al}_{34}\text{Au}_{51}$ is robust against hydrostatic pressure.^{8,10)} By applying pressure up to $P \sim 1.54$ GPa, critical behavior in physical quantities shown in Table I does not change. To get insight into the above fundamental question, here we try to understand the reason why robust criticality appears in $\text{Yb}_{15}\text{Al}_{34}\text{Au}_{51}$ under pressure.

Thus the aim of this Letter is to clarify the key mechanism of the robustness of quantum criticality from the viewpoint of quantum valence criticality. Since the locality of valence fluctuation, i.e., charge transfer between the 4f electron at Yb and conduction electrons at surrounding atoms is considered to be important, we focus on the Yb-Al-Au cluster which is the basic unit of the quasicrystal. We show that quantum critical regime of valence fluctuations is extended to wide region in the phase diagram, which well explains robust criticality observed in $\text{Yb}_{15}\text{Al}_{34}\text{Au}_{51}$ under pressure.

Let us start our discussion by analyzing the Yb-Al-Au cluster. Figure 1 shows concentric

Table I. New type of quantum criticality in uniform magnetic susceptibility χ , NMR/NQR relaxation rate $(T_1T)^{-1}$, specific-heat coefficient C/T , and resistivity ρ . As for valence criticality, $T \gg T_0$ regime with T_0 being characteristic temperature of critical valence fluctuation is shown (see⁷⁾ for detail).

Material/Theory	χ	$(T_1T)^{-1}$	C/T	ρ
YbRh_2Si_2 ⁵⁾	$T^{-0.6}$	$T^{-0.5}$	$-\ln T$	T
$\beta\text{-YbAlB}_4$ ⁶⁾	$T^{-0.5}$	-	$-\ln T$	$T^{1.5} \rightarrow T$
$\text{Yb}_{15}\text{Al}_{34}\text{Au}_{51}$ ⁸⁾	$T^{-0.51}$	$\propto \chi$	$-\ln T$	T
Valence criticality ⁷⁾	$T^{-0.5\sim-0.7}$	$\propto \chi$	$-\ln T$	T

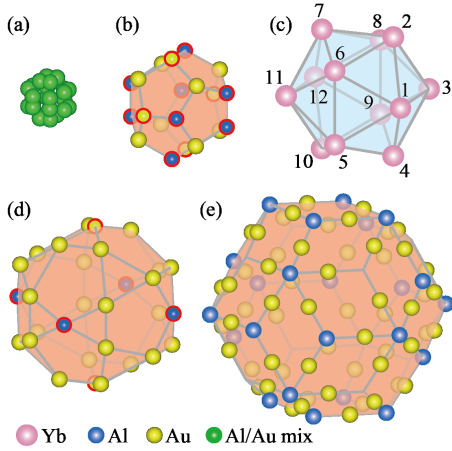


Fig. 1. (color online) Concentric shell structures of Tsai-type cluster in the Yb-Al-Au approximant: (a) first shell, (b) second shell, (c) third shell, (d) fourth shell, and (e) fifth shell. The number in (c) indicates the i -th Yb site.

shell structures of Tsai-type cluster in the Yb-Al-Au approximant, which is the basic structure of the quasicrystal $\text{Yb}_{15}\text{Al}_{34}\text{Au}_{51}$.⁸⁾ The approximant has periodic arrangement of the body-centered cubic structure whose unit cell contains the shell structures shown in Fig. 1(a)-(e). In the second shell, 12 sites are the Al/Au mixed sites (the sites framed in red in Fig. 1(b)) where the Al or Au atom exists with the rate of 62 %/38 %, respectively.¹¹⁾ In the fourth shell, 6 sites are the Al/Au mixed sites (the sites framed in red in Fig. 1(d)) where the Al or Au atom exists with the rate of 59 %/41 %, respectively.¹¹⁾ These rates are average values of the whole crystal. Hence the location of the Al and Au sites and the existence ratio can be different at the next-to-next concentric shells each other both in the quasicrystal and approximant. Thus the 2nd and 4th shells illustrated in Figs. 1(b) and 1(d), respectively, are such examples.

As noted above, almost dispersionless critical valence fluctuation mode is the key origin of emergence of the new type of quantum criticality shown in Table I. This implies that locality of valence fluctuation is essentially important. Namely, charge transfer between the Yb site and surrounding atoms is considered to play a key role, which is basically local. Hence we concentrate on the Yb-Al-Au cluster shown in Fig. 1.

To construct a minimal model, we employ the result of recent experiment in $\text{Yb}_{15}\text{Al}_{34}\text{Au}_{51}$.¹⁰⁾ The same measurement as in Table I performed by replacing Al with Ga has revealed that quantum critical behavior in the physical quantities disappears. This sug-

gests that conduction electrons at the Al site contribute to the quantum critical state. Hence we consider a simplest minimal model for the 4f-hole orbital at the Yb site and conduction-hole orbital at the Al site:

$$\begin{aligned}
H = & - \sum_{\alpha=2,5} \sum_{\langle \xi \nu \rangle \sigma}^{(\alpha)} t_{\xi \nu}^{(\alpha)} (c_{\xi \sigma}^\dagger c_{\nu \sigma} + \text{h.c.}) - \sum_{\xi \sigma}^{(4)} \sum_{\eta}^{(5)} t_{\xi \eta} (c_{\xi \sigma}^\dagger c_{\eta \sigma} + \text{h.c.}) \\
& + \varepsilon_f \sum_{i=1\sigma}^{12} n_{i\sigma}^f + U \sum_{i=1}^{12} n_{i\uparrow}^f n_{i\downarrow}^f + \sum_{i=1\sigma}^{12} \sum_{\eta}^{(2,4,5)} V_{i\eta} (f_{i\sigma}^\dagger c_{\eta \sigma} + \text{h.c.}) \\
& + U_{fc} \sum_{i=1\sigma}^{12} \sum_{\eta \sigma'}^{(2,4)} n_{i\sigma}^f n_{\eta \sigma'}^c
\end{aligned} \tag{1}$$

where $f_{j\sigma}^\dagger$ ($f_{j\sigma}$) and $c_{j\sigma}^\dagger$ ($c_{j\sigma}$) are creation (annihilation) operators of the f hole and the conduction hole at the j -th site with spin σ , respectively, and $n_{j\sigma}^f \equiv f_{j\sigma}^\dagger f_{j\sigma}$ and $n_{j\sigma}^c \equiv c_{j\sigma}^\dagger c_{j\sigma}$. The first term represents the conduction-hole transfer on the 2nd and 5th shells, where $\sum_{\langle \xi \nu \rangle}^{(\alpha)}$ denotes the summation of the nearest-neighbor Al sites on the α -th shell ($\alpha=2$: Fig. 1(b) and $\alpha=5$: Fig. 1(e)). The second term represents the conduction-hole transfer between the 4th and 5th shells, where $\sum_{\xi \sigma}^{(4)} \sum_{\eta}^{(5)}$ denotes the summation of the nearest-neighbor Al sites on the 5th shell for each Al site on the 4th shell (Fig. 1(d)). The third and fourth terms represent the f-hole energy level ε_f and onsite Coulomb repulsion U on the 3rd shell (Fig. 1(c)), respectively. The fifth term represents the hybridization $V_{i\eta}$ between f and conduction holes, where $\sum_{i=1\sigma}^{12} \sum_{\eta}^{(\alpha)}$ denotes the summation of the nearest-neighbor sites on the α -th shell ($\alpha=2, 4$, or 5) for each i -th Yb site on the 3rd shell.

The last term represents the inter-orbital Coulomb repulsion U_{fc} . This term has been shown theoretically to be essentially important to cause the quantum criticality of Yb-valence fluctuations.^{7,12)} We note that in YbRh₂Si₂, Yb 3d-4f resonant photoemission measurement has revealed recently that Yb 5d electrons contribute to the energy band located at the Fermi level.¹³⁾ This strongly suggests importance of inter-orbital Coulomb repulsion between the 4f and 5d states due to its onsite nature. As for Yb₁₅Al₃₄Au₅₁, we expect that charge transfer between 4f and conduction states is also considerably influenced by the Yb 5d state which is considered not only to contribute to U_{fc} but also to hybridize with the conduction states at surrounding atoms since 5d wave function is spreading to a certain extent. Here, we introduced the U_{fc} term between the 3rd (Yb) shell and the conduction states at the surrounding Al sites to express this effect most simply as in eq. (1) instead of introducing the 5d orbital at each Yb site explicitly. We note that quantum valence criticality in Table I is shown to appear on the basis of the periodic Anderson model with the U_{fc} term whose structure is essentially

the same as eq. (1).⁷⁾

Emergence of heavy-electron behavior in $\text{Yb}_{15}\text{Al}_{34}\text{Au}_{51}$ is ascribed to the strong Coulomb repulsion U working on-site 4f holes at the Yb site. To determine the ground-state phase diagram of the model eq. (1), here we employ the slave-boson mean-field approach in the limit of strong hole correlation, $U = \infty$,¹⁴⁾ as a first step of analysis. To describe the state for $U = \infty$, we consider $Vf_{i\sigma}^\dagger b_i c_{\eta\sigma}$ instead of $Vf_{i\sigma}^\dagger c_{\eta\sigma}$ in eq. (1) by introducing the slave-boson operator b_i at the i -th site to describe the f^0 state and require the constraint $\sum_{i=1}^{12} \lambda_i (\sum_{\sigma} n_{i\sigma}^f + b_i^\dagger b_i - 1)$ with λ_i being the Lagrange multiplier. We employ the mean-field treatment as $\bar{b}_i = \langle b_i \rangle$. For the U_{fc} term in eq. (1), we employ the mean-field decoupling as $n_{i\sigma}^f n_{\eta\sigma'}^c \approx n_{i\sigma}^f \langle n_{\eta\sigma'}^c \rangle + \langle n_{i\sigma}^f \rangle n_{\eta\sigma'}^c - \langle n_{i\sigma}^f \rangle \langle n_{\eta\sigma'}^c \rangle$. By optimizing the ground-state energy with respect to λ_i and \bar{b}_i , $\partial \langle H \rangle / \partial \lambda_i = 0$ and $\partial \langle H \rangle / \partial \bar{b}_i = 0$, we obtain a set of the mean-field equations.

$$\sum_{\sigma} \langle f_{i\sigma}^\dagger f_{i\sigma} \rangle + \bar{b}_i^2 = 1, \quad (2)$$

$$\sum_{\eta\sigma}^{(2,4,5)} V_{i\eta} \langle f_{i\sigma}^\dagger c_{\eta\sigma} \rangle + \lambda_i \bar{b}_i = 0, \quad (3)$$

for $i = 1, \dots, 12$.

Since we now consider the Yb-Al-Au cluster without periodic lattice structure, Fourier transformation to momentum space which diagonalizes the mean-field Hamiltonian is not available to solving eqs. (2) and (3). Here we calculate them by using the Slater matrix as follows.

The ground state of the mean-field Hamiltonian obtained from eq. (1) is given by $|\phi\rangle = |\phi_\uparrow\rangle \otimes |\phi_\downarrow\rangle$ with $|\phi_\sigma\rangle = \prod_{k=1}^{N_\sigma} \left(\sum_{j=1}^N \phi_{jk}^\sigma a_{j\sigma}^\dagger \right) |0\rangle$, where N is the total number of sites and N_σ the total number of holes with σ spin in the system. Here, ϕ_{jk}^σ is the $N \times N_\sigma$ Slater matrix constituted of the N_σ eigen vectors with the N dimension, which corresponds to the eigen values of the $N \times N$ mean-field Hamiltonian matrix from the lowest one to the N_σ -th lowest one. The creation operator $a_{j\sigma}^\dagger$ is given by $f_{j\sigma}^\dagger (c_{j\sigma}^\dagger)$ at the j -th site in the 3rd shell (the 2nd, 4th, and 5th shell) in Fig. 1. The expectation value of product of $a_{j\sigma}^\dagger$ and $a_{l\sigma}$ is calculated as

$$G_{jl\sigma} = \frac{\langle \phi_\sigma | a_{j\sigma}^\dagger a_{l\sigma} | \phi_\sigma \rangle}{\langle \phi_\sigma | \phi_\sigma \rangle} = \sum_{j'=1}^N \sum_{l'=1}^{N_\sigma} \phi_{jj'}^\sigma g_{j'l'} \phi_{l'\sigma}^\sigma, \quad (4)$$

where the matrix g is given by $g \equiv ({}^t \phi^\sigma \phi^\sigma)^{-1}$. By using eq. (4), $\langle f_{i\sigma}^\dagger f_{i\sigma} \rangle$ and $\langle f_{i\sigma}^\dagger c_{\eta\sigma} \rangle$ in eqs. (2) and (3) are calculated. The calculation scheme is summarized as follows: 1) First we assume a set of the mean fields λ_i and \bar{b}_i for $i = 1, \dots, 12$. 2) Then the mean-field Hamiltonian is set. 3) By diagonalizing the Hamiltonian matrix, we obtain the N_σ eigen vectors corresponding

to the eigen values from the lowest one to the N_σ -th lowest one, which constitute the Slater matrix ϕ^σ . 4) By using eq. (4), we calculate totally 24 mean-field equations of eqs. (2) and (3). 5) By using the multi-variable Newton method or the iterative method, we obtain the set of mean-fields λ_i and \bar{b}_i for $i = 1, \dots, 12$ for the next step. The above procedure from 1) to 5) is repeated until the mean-fields which satisfy eqs. (2) and (3) within the required accuracy are obtained.

We consider the case that Al atoms are located at the Al/Au mixed sites in the 2nd shell and 4th shell with inversion symmetry with respect to the cluster center as shown in Figs. 1(b) and 1(d), respectively. Due to this symmetry, the number of the mean fields can be reduced from 12 to 6 for λ_i and \bar{b}_i , which makes calculation simpler.

To understand the fundamental nature of this system, here we set $t_{\xi\nu}^{(2)} = t_{\xi\nu}^{(5)} = t_{\xi\eta} = t = 1$, $V_{in} = V = 0.3$, and $U = \infty$ for a typical parameter set of heavy electron systems, as a first step of analysis. We consider the case that the total hole number $(N_\uparrow, N_\downarrow) = (24, 24)$ in the Yb-Al-Au cluster with $N = 54$ Yb and Al atoms in total, as shown in Fig. 1. By calculating the ε_f dependence of $\langle n_i^f \rangle = \langle n_{i\uparrow}^f \rangle + \langle n_{i\downarrow}^f \rangle$ for each U_{fc} in the atomic configuration shown in Fig. 1, the valence susceptibility defined by $\chi_{vi} \equiv -\partial\langle n_i^f \rangle / \partial\varepsilon_f$ is obtained, as shown in Fig. 2.

This result can be understood qualitatively on the basis of the mean-field picture, as follows. Let us focus on the single f orbital at the i -th site on the 3rd shell (see Fig. 1(c)). When the f level is located at a deep position, i.e., ε_f is small enough in eq. (1), one f hole is located at the i -th site with $\langle n_i^f \rangle = 1$, as a result of on-site strong hole correlations caused by $U = \infty$. As U_{fc} increases, at the point which satisfies

$$\varepsilon_f + U_{fc} \sum_{\eta}^{(2,4)} \langle n_{\eta}^c \rangle \approx \mu, \quad (5)$$

with μ being the chemical potential, $\langle n_i^f \rangle$ shows a jump to the smaller $\langle n_i^f \rangle$ value. Namely, first-order valence transition (FOVT) occurs since large U_{fc} forces holes pour into either the f level or the conduction orbital. As ε_f increases or U_{fc} decreases along the FOVT line, the value of the valence jump decreases and finally disappears at the quantum critical end point of the FOVT. This point is called the quantum critical point of the valence transition (VQCP), at which critical valence fluctuation diverges, i.e., $\chi_{vi} = \infty$. As further ε_f increases or U_{fc} decreases along the valence-crossover line extended from the FOVT line, the valence susceptibility χ_{vi} is still enhanced, giving rise to the quantum critical regime in the ε_f - U_{fc} plane. Intuitively, critical valence fluctuations are enhanced around the valence-crossover line near the VQCP because of the enhanced possibility whether for holes to stay at the f level or

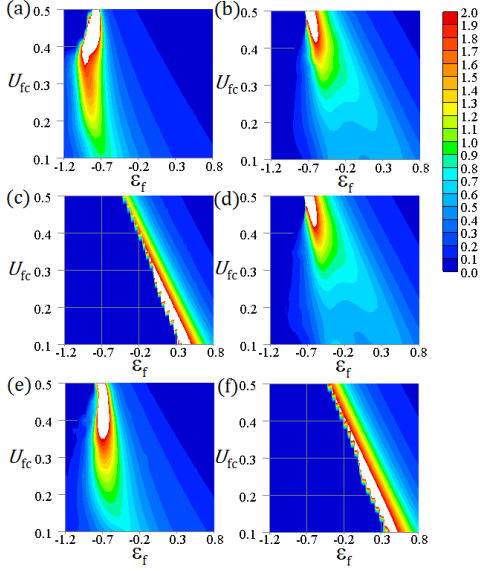


Fig. 2. (color online) Contour plot of valence susceptibility χ_{vi} for (a) $i=1$, (b) 2, (c) 3, (d) 4, (e) 5, and (f) 6 in the ε_f - U_{fc} plane. Each white region shows diverging critical valence fluctuation arising from the VQCP for each i .

to move up to the Fermi level to avoid the energy loss due to U_{fc} (see eq. (5)).

When V is set to be the larger value, the location of the VQCP is shifted to the smaller- ε_f and larger- U_{fc} direction in the ε_f - U_{fc} phase diagram since larger V promotes charge transfer between f level and conduction states. In the case of the smaller V , the VQCP is shifted to the larger- ε_f and smaller- U_{fc} direction.

Now let us consider the 6 f -orbitals on the i -th site ($i=1\sim 6$) on the 3rd shell (see Fig. 1(c)). Since Al is located with a certain rate at the Al/Au mixed sites on the 2nd and 4th shells, as shown in Figs. 1(b) and 1(d), respectively, each f site is not equivalent. For instance, let us focus on the c - f hybridization between the 2nd and 3rd shells. As seen in Figs. 1(b) and 1(c), the f orbital at the $i=1$ Yb site hybridizes with the conduction orbitals at the three Al sites on the 2nd shell. On the other hand, the f orbital at the $i=6$ Yb site only hybridizes with the conduction orbital at one Al site on the 2nd shell. Other f orbitals at the i -th Yb site for $i = 2, 3, 4$, and 5 have the hybridization paths on the 2nd shell in between. Namely, “effective c - f hybridization strength” with the 2nd, 4th, and 5th shells is different each other for the $i=1\sim 6$ Yb sites.

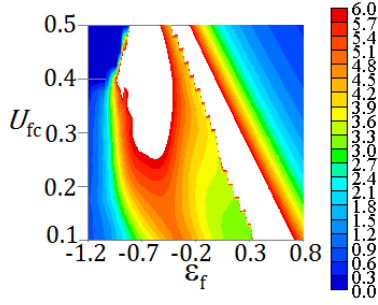


Fig. 3. (color online) Contour plot of total valence susceptibility $\chi_v = \sum_{i=1}^{12} \chi_{vi}$ in the ε_f - U_{fc} plane. White regions represent diverging critical valence fluctuations arising from the VQCP's for $i = 1 \sim 12$. Note that contour values are shown in larger scale than that in Fig. 2.

As ε_f increases from a deep position, $\langle n_1^f \rangle$ first changes at the FOVT as well as valence-crossover line (see Fig. 2(a)) since the effective c-f hybridization is strongest among $i=1\sim 6$. When ε_f exceeds the FOVT or valence-crossover line for $i = 1$, charge transfer from the f orbital at the $i = 1$ Yb site to the conduction orbitals at the surrounding Al sites occurs. Then the Fermi energy μ in eq. (5) is determined under the rearrangement of total holes in this system. As ε_f further increases, charge transfer occurs similarly when eq. (5) is satisfied for μ set under the rearranged total holes for $i = 5, 4, 2$, and 3, as shown in Figs. 2(e), 2(d), 2(b), and 2(c), respectively. Finally, the f orbital at the $i = 6$ Yb site which has the smallest effective c-f hybridization shows the FOVT with the VQCP, as shown in Fig. 2(f).

An important result is that VQCP's appear as islands in the ε_f - U_{fc} phase diagram as shown in Fig. 2, which makes critical regime enlarged. Actually, total valence susceptibility $\chi_v \equiv \sum_{i=1}^{12} \chi_{vi}$ shown in Fig. 3 corresponding to experimental observation of criticality exhibit that critical valence fluctuations arising from each VQCP spot located closely are unified and hence the wide quantum critical regime appears in the ε_f - U_{fc} plane. Note that although we now consider the case with inversion symmetry on the Al sites (see Fig. 1), in reality, absence of the symmetry gives rise to 12 VQCP spots but not 6 spots per an Yb-Al-Au cluster. This makes the critical regime be further enlarged in the ε_f - U_{fc} phase diagram.

When pressure is applied to Yb-based materials, electrons located at the surrounding atoms approach the tail of wavefunction of the 4f electron at Yb, which makes the energy level

of the crystalline electronic field increase.¹⁵⁾ In the hole picture, this corresponds to decrease in ε_f in eq. (1). Since U_{fc} is considered to increase under pressure in general, applying pressure to the Yb-based system corresponds to moving on the line toward the left-increasing direction in the ε_f - U_{fc} phase diagram in Fig. 3. Then in case that applying pressure follows the line in the enhanced critical regime, robust criticality is realized, which offers an explanation for robust criticality observed in $\text{Yb}_{15}\text{Al}_{34}\text{Au}_{51}$ under pressure.⁸⁾

Present analysis provides the core model both for quasicrystal and approximant: By further considering outer concentric shells in Fig. 1, quasicrystal structure is constructed, while by considering periodic arrangement of the concentric shells in Fig. 1 as a unit cell, approximant is constructed. Although comparison of the electronic states in the bulk limit of both systems should be made for complete understanding of each system, the fundamental properties clarified here are considered to be unchanged even in the bulk limit since valence fluctuation is ascribed to atomic origin so that locality is essential. Namely, our result seems to be applied not only to systems with quasi-periodicity but also to those with periodicity of the lattice arrangement. Here we point out a possibility that difference in critical behavior between quasicrystal and approximant⁸⁾ may be ascribed to the location of the phase diagram: The former is located in the enhanced critical valence fluctuation regime as noted above and the latter seems slightly away from it.

Emergence of a wide critical regime in the phase diagram offers a natural explanation for why quantum critical behavior was observed in materials without tuning control parameters in Table I. As for β - YbAlB_4 , four Yb atoms are located in the unit cell, which can be an origin of the robust criticality in this material, similarly to the above results. Here we note that rather short distance between Yb atoms along the c axis ($\sim 3.4 \text{ \AA}$)⁶⁾ is considered to contribute to the robust criticality. The Yb-Yb transfer via the conduction state at the B site promotes to widen the critical valence fluctuation regime in the phase diagram. We confirmed this tendency by the calculation in the periodic Anderson model with the U_{fc} term taking into account the effect of the f-f transfer. This can be understood intuitively as relaxation of the valence-fluctuating condition of eq. (5) since ε_f has a certain width due to the f-f transfer effect.

To summarize, we have shown that robust criticality of valence fluctuation can appear in Yb-based heavy electron systems under ambient as well as applied pressure. This mechanism is considered to play a key role in $\text{Yb}_{15}\text{Al}_{34}\text{Au}_{51}$ and is expected to have broader applicability also in the other Yb- and Ce-based heavy electron systems.

Acknowledgment

We thank N. K. Sato, T. Ishimasa, K. Deguchi, and T. Watanuki for valuable discussions about experimental data. One of us (S.W.) is supported by JASRI (Proposal Nos. 2012B0046 and 2013A0046). This work is supported by the Grant-in-Aid for Scientific Research (No. 24540378 and No.25400369) from the Japan Society for the Promotion of Science (JSPS).

References

- 1) T. Moriya: *Spin Fluctuations in Itinerant Electron Magnetism* (Springer-Verlag, Berlin, 1985).
- 2) T. Moriya and T. Takimoto: J. Phys. Soc. Jpn. **64** (1995) 960.
- 3) J. A. Hertz: Phys. Rev. B **14** (1976) 1165.
- 4) A. J. Millis: Phys. Rev. B **48** (1993) 7183.
- 5) P. Gegenwart, J. Custers, Y. Tokiwa, C. Geibel, and F. Steglich: Phys. Rev. Lett. **94** (2005) 076402, and references therein.
- 6) Y. Matsumoto, S. Nakatsuji, K. Kuga, Y. Karaki, N. Horie, Y. Shimura, T. Sakakibara, A. H. Nevidomskyy, and P. Coleman: Science **331** (2011) 316, and references therein.
- 7) S. Watanabe and K. Miyake: Phys. Rev. Lett. **105** (2010) 186403.
- 8) K. Deguchi, S. Matsukawa, N. K. Sato, T. Hattori, K. Ishida, H. Takakura, and T. Ishimasa: Nature Mat. **11** (2012) 1013.
- 9) T. Watanuki, S. Kashimoto, D. Kawana, T. Yamazaki, A. Machida, Y. Tanaka, and T. J. Sato: Phys. Rev. B **86** (2012) 094201.
- 10) N. K. Sato and K. Deguchi: private communications.
- 11) T. Ishimasa, Y. Tanaka, and S. Kashimoto: Phil. Mag. **91** (2011) 4218.
- 12) K. Miyake: J. Phys.: Condens. Matter **19** (2007) 125201.
- 13) A. Yasui, Y. Saitoh, S.-I. Fujimori, I. Kawasaki, T. Okane, Y. Takeda, G. Lapertot, G. Knebel, T. D. Matsuda, Y. Haga, and H. Yamagami: Phys. Rev. B **87** (2013) 075131.
- 14) N. Read and D. M. Newns: J. Phys. C: Solid State Phys. **16** (1983) 3273.
- 15) S. Watanabe and K. Miyake: J. Phys.: Condens. Matter **23** (2011) 094217.